

# EES Solar

Accepted Manuscript

This article can be cited before page numbers have been issued, to do this please use: J. P. Medina Flechas, D. Barrit, R. patel, T. Li, E. Cariou, M. Provost, L. Kopprio, S. Le Gall, J. Kleider, O. Almora, C. Bainier, P. Lopez-Varo and P. Schulz, *EES Sol.*, 2026, DOI: 10.1039/D6EL00034G.



This is an Accepted Manuscript, which has been through the Royal Society of Chemistry peer review process and has been accepted for publication.

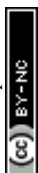
Accepted Manuscripts are published online shortly after acceptance, before technical editing, formatting and proof reading. Using this free service, authors can make their results available to the community, in citable form, before we publish the edited article. We will replace this Accepted Manuscript with the edited and formatted Advance Article as soon as it is available.

You can find more information about Accepted Manuscripts in the [Information for Authors](#).

Please note that technical editing may introduce minor changes to the text and/or graphics, which may alter content. The journal's standard [Terms & Conditions](#) and the [Ethical guidelines](#) still apply. In no event shall the Royal Society of Chemistry be held responsible for any errors or omissions in this Accepted Manuscript or any consequences arising from the use of any information it contains.

## Broader Context Statement

Perovskite solar cells (PSCs) hold immense promise for next-generation photovoltaic technologies, offering high efficiency and cost-effective manufacturing. However, their widespread deployment is hindered by fundamental challenges related to charge transport, interfacial recombination, and ion migration—factors that significantly affect device stability and performance. Our study presents an advanced characterization approach combining J-V, SunsVoc, and impedance spectroscopy (IS) with multi-biasing analysis to disentangle the effects of mobile ions and energetic band offsets at perovskite/contact interfaces in inverted (p-i-n) architectures. By integrating experimental IS data with drift-diffusion (DD) simulations, we provide deeper physical insights into charge carrier dynamics, recombination mechanisms, and interfacial selectivity. Our findings reveal that high energetic band offsets at charge transport layers (CTLs) can limit fill factor (FF) and open-circuit voltage (VOC), while ionic accumulation modulates capacitive and recombination behavior. Understanding these complex interdependencies is crucial for overcoming efficiency bottlenecks and enhancing long-term PSC stability, paving the way for the optimization of next-generation tandem and scalable perovskite-based solar technologies.



# Characterization of Ionic-electronic Transport and Recombination in Perovskite Solar Cells under Multi-biasing Conditions

View Article Online  
DOI: 10.1002/ael.202300034G

Juan Pablo Medina Flechas<sup>1,2\*</sup>, Dounya Barrit<sup>1,2</sup>, Raj Dashrath Patel<sup>2</sup>, Tianfang Li<sup>1,2</sup>, Estelle Cariou<sup>2</sup>, Marion Provost<sup>2</sup>, Leonardo Kopprio<sup>2,3</sup>, Sylvain Le Gall<sup>2,3</sup>, Jean-Paul Kleider<sup>2,3</sup>, Osbel Almora<sup>4</sup>, Camille Bainier<sup>1,2</sup>, Pilar López-Varo<sup>2\*</sup>, Philip Schulz<sup>2,5\*</sup>

<sup>1</sup> TotalEnergies OneTech, 91120 Palaiseau, France

<sup>2</sup> Institut Photovoltaïque d'Ile-de-France (IPVF), 18 Boulevard Thomas Gobert, 91120 Palaiseau, France

<sup>3</sup> Université Paris-Saclay, CentraleSupélec, CNRS, Laboratoire de Génie Electrique et Electronique de Paris, 91192 Gif-sur-Yvette, France

<sup>4</sup> Department of Electronic, Electrical and Automatic Engineering, Universitat Rovira i Virgili, 43007 Tarragona, Spain

<sup>5</sup> Institut Photovoltaïque d'Ile-de-France (IPVF), UMR 9006, CNRS, Ecole Polytechnique - IP Paris, Chimie Paristech - PSL, 18 Boulevard Thomas Gobert, Palaiseau 91120, France

\* [medina.juanpablo@outlook.es](mailto:medina.juanpablo@outlook.es)

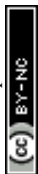
\* [pilar.lopez-varo@ipvf.fr](mailto:pilar.lopez-varo@ipvf.fr)

\* [philip.schulz@cnrs.fr](mailto:philip.schulz@cnrs.fr)

## Abstract

Perovskite solar cells (PSCs) are among the most promising photovoltaic technologies, offering high efficiencies and low fabrication costs. However, their commercialization remains limited by stability issues and incomplete understanding of the intrinsic mechanisms governing device performance. Particularly, slow mobile-ion dynamics can modulate charge recombination and extraction, strongly affecting device operation. Here, we use impedance spectroscopy (IS) to investigate the underlying processes that govern the current-voltage ( $J$ - $V$ ) response of PSCs under operational conditions. To this end, we combine  $J$ - $V$ , SunsVoc and IS measurements using a multi-bias approach to analyze p-i-n PSCs under short-circuit (SC) and open-circuit (OC) conditions over a wide range of illumination intensities. Complementary, drift-diffusion (DD) simulations and equivalent circuit model (ECM) analysis on IS under SC conditions enable extraction of key transport properties, including carrier mobilities, mobile ion concentration, and shunt resistance. The role of mobile ion concentration is analyzed for both regimes. Across the simulated parameter space, the low-frequency dark resistance is determined by the shunt resistance, and nearly independent of recombination rates or mobile ion concentration. Therefore, the associated dark low-frequency RC time constant cannot be directly interpreted as a recombination lifetime. Under OC conditions, we further evaluate the coupled effects of ionic motion and energy band offsets on recombination, comparing the ideality factor derived across techniques. This integrated experimental–theoretical framework provides deeper insight into the electronic and ionic processes governing PSC performance.

**Key words:** Photovoltaics, Halide Perovskites, Impedance Spectroscopy, Electronic Properties, Ion Migration.



## Introduction

Perovskite solar cells (PSC) are arguably the emerging photovoltaic (PV) technology of the decade, recently achieving certified power conversion efficiencies (*PCE*) of 27.3% and 34.8% for single junction and silicon/perovskite tandem devices, respectively<sup>[1]</sup>. Their exceptional optoelectronic properties, including high absorption coefficients, long carrier diffusion lengths, defect tolerance, and tunable bandgap ( $E_g$ ),<sup>[2]</sup> combined with low-temperature processability make them strong candidates for large scale industrialization<sup>[2–4]</sup>. However, their limited long-term stability remains a challenge<sup>[5]</sup>. A major factor underlying this instability is the presence of mobile ions within the perovskite absorber, whose redistribution under electrical bias and illumination modifies the internal electric field and affects charge-carrier dynamics.

Standard photovoltaic characterization methods, including current density-voltage (*J-V*) and  $\text{SunsV}_{\text{OC}}$  measurements, are routinely employed to evaluate device performance and infer recombination mechanisms<sup>[6–9]</sup>. Their interpretation typically relies on the assumption of fast electronic charge-carrier response under steady-state conditions<sup>[10,11]</sup>. In PSCs, however, this assumption is frequently invalidated by slow ionic motion. The measured optoelectronic response reflects a convolution of electronic transport and recombination with bias-dependent effective built-in potentials ( $V_{\text{bi}}$ )<sup>[12]</sup>, contact instabilities<sup>[13–16]</sup>, interfacial band offsets<sup>[7,17]</sup> and electric field screening due to mobile ion redistribution within the perovskite (PK) layer<sup>[18–20]</sup>. Among these, ionic accumulation at PK/charge transport layer (CTL) interfaces can dynamically reshape recombination pathways, impede charge extraction, and induce *J-V* hysteresis<sup>[21]</sup>. Consequently, the ideality factor from *J-V* or  $\text{SunsV}_{\text{OC}}$  measurements alone provides limited insight into underlying losses. Decoupling these coupled electronic and ionic processes requires characterization techniques capable of resolving distinct temporal scales, supported by physical interpretation via drift-diffusion (DD) simulations<sup>[22,23]</sup>.

Impedance spectroscopy (IS) is a powerful method to probe these coupled dynamics in the frequency domain. PSCs exhibit characteristic impedance features spanning multiple decades in frequency, reflecting fast electronic processes in the PK bulk and slower ionic redistribution and interfacial charge accumulation<sup>[24,25]</sup>. The strong coupling between these processes produces complex spectra, including pronounced low-frequency capacitances and bias-dependent resistive elements. Multiple equivalent electric circuit models (ECMs) have been proposed to interpret these responses<sup>[25–29]</sup>, mainly depending on the given operating



condition such as voltage bias and light illumination at short-circuit (SC), maximum power point (MPP) or open-circuit (OC); as well as, on device-specific factors including composition and degree of degradation. The use of general ECMs, for the interpretation of IS spectra in PSCs, remains limited. A unified physical understanding of IS in PSCs therefore requires models that incorporate coupled electronic and ionic transport across operating conditions.

Bias-dependent IS offers complementary insight into dominant device physics. Under SC conditions, the impedance response primarily reflect charge transport and extraction processes<sup>[30]</sup>. Under OC conditions, the IS response is governed by recombination and diffusion-driven mobile ionic redistribution <sup>[20,24,25]</sup>. This is due to the device operating at zero current flow and near to flat-band conditions in the case of standard one sun illumination (open circuit voltage close to the  $V_{bi}$ ). At MPP, the high nonlinearity in the  $J-V$  response, with the overlapping of charge transport-recombination and extraction, complicates the interpretation of IS spectra. Although IS in PSCs has been widely studied under OC<sup>[31–33]</sup> and, more recently, under SC conditions<sup>[30]</sup>, a unified framework that consistently combines both regimes and direct comparison to DD simulations remains limited. In this context, a multi-bias approach is essential to resolve the coupled effects of electric field screening, recombination, and ionic dynamics, which is the focus of this study.

In this work, we present a comprehensive opto-electric characterization methodology for PSCs, combining  $J-V$ , SunsVoc and IS with a multi-biasing approach to quantitatively resolve coupled electronic–ionic effects in PSCs. Using an inverted (p-i-n) architecture as case study, IS measurements are performed under SC and OC conditions at a wide range of illumination intensities. To enable a physically grounded interpretation, experimental spectra are analyzed using equivalent ECM and compared with the ECM fitting of the one-dimensional DD simulations performed with the open source *Driftfusion* code<sup>[34]</sup>. To the best of our knowledge, this work provides the first study integrating both OC and SC regimes through combined experimental and DD simulations. In particular, we analyze the IS data through the representation of resistive and capacitive elements as function of short-circuit current density ( $J_{SC}$ ) and open-circuit voltage ( $V_{OC}$ ). First, DD simulations are used to evaluate the impact of key device parameters, with particular emphasis on mobile ion concentration, and to identify new correlations with high- and low-frequency resistive components. We analyze the effect of field screening and IS response difference between SC and OC. Subsequently, the combined experimental–numerical framework enables extraction of key physical parameters, including



carrier mobility ( $\mu_{PK}$ ), mobile ion concentration ( $N_{ion}$ ), and the shunt resistance ( $R_{SH}$ ), from SC measurements. In addition, ideality factors ( $n_{id}$ ) derived from dark  $J-V$  and Suns- $V_{OC}$  analysis are compared with those obtained from OC impedance, establishing a consistent framework for assessing dominant recombination pathways. This approach further enables evaluation of the coupled effects of mobile ions and interfacial energy band offsets at perovskite/CTL interfaces.

## Results and discussion

In this work, we analyzed PSCs with an inverted (p-i-n) configuration that were fabricated on FTO/glass substrates with the structure glass/FTO/ $NiO_x$ /perovskite/ $C_{60}$ /SnO<sub>2</sub>/Au, as depicted in **Figure 1 (a)**. First, dynamic light  $J-V$  curves were measured at 1 sun equivalent illumination and compared with DD simulations using the one-dimensional *Driftfusion* code (see simulated device structure in **Fig. 1 (b)**). For the device performance analysis, we focused on the variation of four key parameters in the PSCs. First, the carrier mobility in the perovskite  $\mu_{PK}$  was varied from 0.2 to 20 cm<sup>2</sup>/Vs, covering the typical range reported in literature [35] with electron and hole mobilities assumed equal for simplicity. Second, the mobile ion concentration  $N_{ion}$  was varied from 10<sup>15</sup> cm<sup>-3</sup> to 10<sup>19</sup> cm<sup>-3</sup> [36,37] considering two mobile ion species (cations and anions) present within the perovskite layer. From the  $JV$  simulations, an ionic concentration close to 10<sup>18</sup> cm<sup>-3</sup> is expected considering the set of fixed device parameters (**Fig. 1 (c)**). Further details regarding device fabrication, parameter selection (Table S1), and simulation methodology are provided in Section S1 of the Supporting Information (SI). Third, the energy band offsets and built-in potential ( $V_{bi}$ ) defined as the difference between the anode and cathode work functions  $\phi_a - \phi_c$  (**Fig. 1 (b)**). Interfacial band misalignment can effectively reduce  $V_{bi}$  impacting the  $J-V$  characteristics (see Figure 3). In the simulations,  $V_{bi}$  is modified by varying the valence band offset  $\Delta VB$  at the perovskite/HTL interface, and the conduction band offset  $\Delta CB$  at the perovskite/ETL interface through adjustment of the electron affinity of the respective CTLs. The CTLs are assumed to be highly doped, with their Fermi levels positioned 100 meV from the band edges (conduction band for ETL and valence band for HTL, respectively). For simplicity, metal contacts are fixed as ohmic, and their Fermi Levels are perfectly aligned with the CTL Fermi levels, as an approximation in the DD model (SI section S1). Fourth, bulk recombination is modelled via defect-assisted Shockley–Read–Hall (SRH) processes assuming a single trap level<sup>[34]</sup> characterized by equal electron-hole lifetimes ( $\tau_{PK}^{SRH} = \tau_e = \tau_h$ ) in the PK bulk.



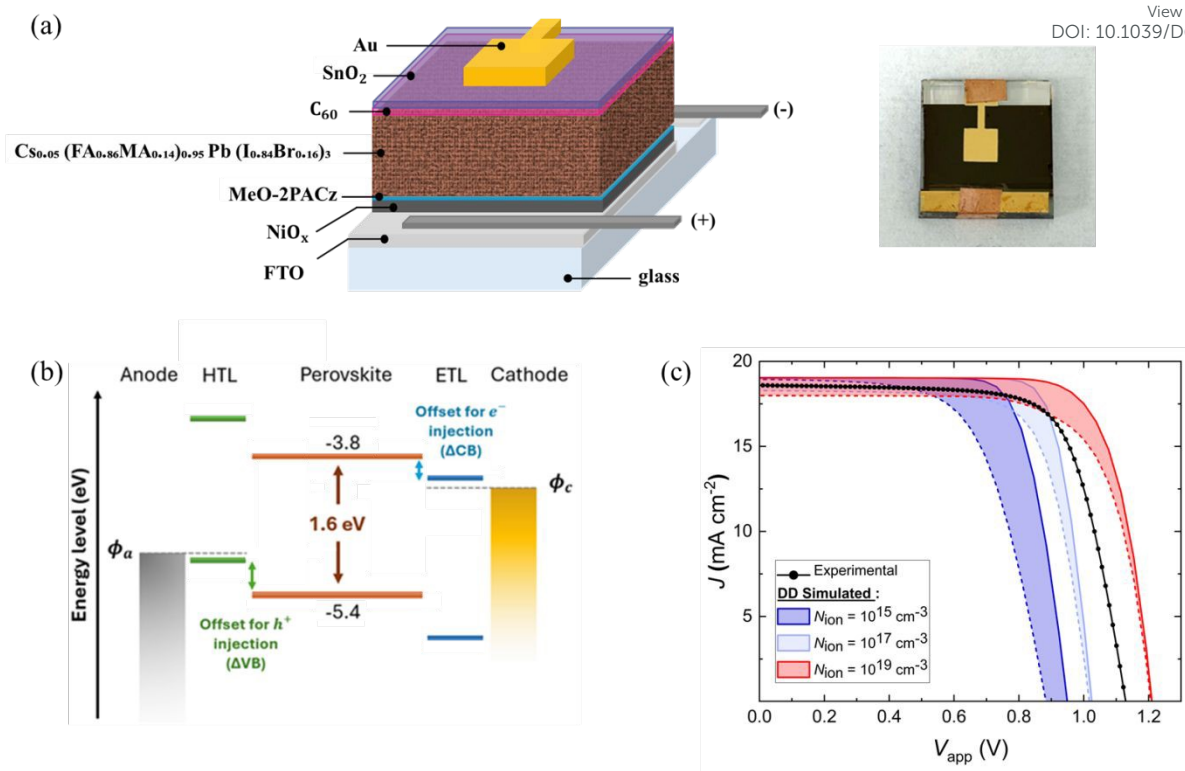
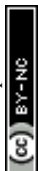


**Figure 1.** (a) PSC schematic vs equivalent top view for a real device, deposited on FTO-glass. (b) Energy levels of one-dimensional structure, before contact equilibrium, defined in DD simulations. (c) Experimental vs DD simulated  $J$ - $V$  curves, varying  $N_{\text{ion}}(\text{cm}^{-3}) = \{10^{15}, 10^{17}, 10^{19}\}$  and  $\mu_{\text{PK}}(\text{cm}^2\text{V}^{-1}\text{s}^{-1}) = \{0.2, 20\}$ , at  $\tau_{\text{PK}}^{\text{SRH}} = 1 \mu\text{s}$  and a low  $V_{\text{bi}} = 0.6 \text{ V}$  ( $\Delta VB = 500 \text{ meV}$  and  $\Delta CB = 300 \text{ meV}$ ). All the  $JV$  scans are simulated and experimentally performed in reverse direction at  $30 \text{ mVs}^{-1}$  and 1 sun equivalent.

After  $JV$  measurements, the IS response was measured under dark and increasing illumination intensity ( $\Psi$ ) from  $10^{-4}$  to 1 sun ( $1000\text{W}/\text{m}^2$ ), in the range of 100 mHz–1 MHz under ambient conditions and at a controlled temperature of  $25 \text{ }^\circ\text{C}$ . Measurements were performed under both SC and OC conditions. The results are shown in **Fig. 2**, in Nyquist plots with real ( $Z'$ ) vs ( $-Z''$ ) imaginary semicircle representation and the corresponding frequency-dependent capacitance Bode plots.

Impedance spectra were fitted to the selected ECM, as shown in the inset of **Fig. 2 (d)**. The model consists of a nested configuration connected in line with a series resistance ( $R_s$ ), accounting for contact and transport-related ohmic losses. Two primary Voigt elements, each comprising a resistor ( $R$ ) in parallel with a capacitive element ( $C$ ), describe the high-frequency (HF) and low-frequency (LF) responses, with characteristic relaxation times  $\tau = RC$ . To account for non-ideal capacitive behaviors arising from interfacial inhomogeneities and material disorder, ideal capacitors were replaced by constant phase elements ( $CPEs$ ), reflecting a distribution of relaxation times rather than a single one<sup>[38]</sup>. The high-frequency semicircle ( $\omega > 1\text{kHz}$ ) is usually attributed to electronic transport-recombination and geometric



capacitance effects of the multilayer device stack. A second semicircle at low frequencies (tens Hz to mHz), is ascribed to additional slow ionic-electronic dynamics and its coupling to interfacial charge accumulation and recombination.

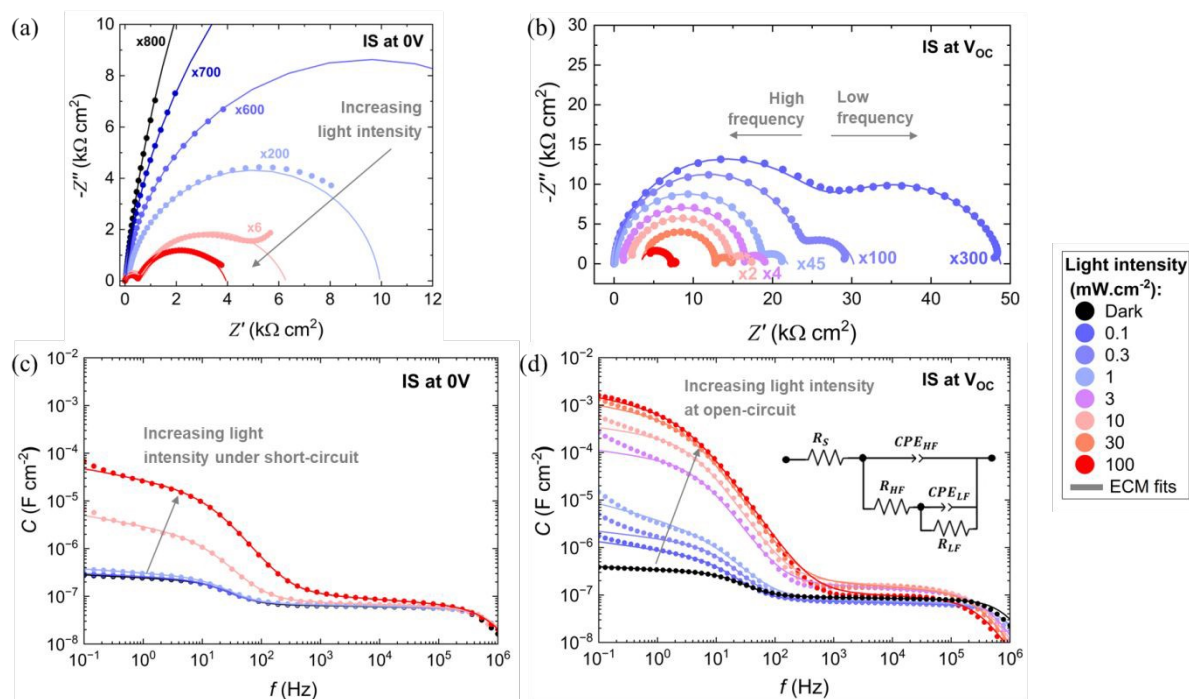
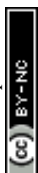


**Figure 2.** IS data increasing  $\Psi$ , measured at SC (a and c) and at OC (b and d) bias conditions, presented in: Nyquist plots (a and b), with real  $Z'$  vs  $-Z''$  imaginary components. Multipliers indicate the required scale-up factor, for full magnitude display, in measurements towards low  $\Psi$  conditions. Bode plots (c and d), with frequency-dependent capacitance. Experimental data (dots) and respective fits (solid lines) to selected ECM, as inset depicted in (d).

The fit values of the individual  $R$  and  $C$  elements were analyzed as a function of  $J_{SC}$  and  $V_{OC}$ . To interpret the experimental results, IS spectra were simulated using DD simulations under equivalent bias and illumination conditions, while varying key device parameters, particularly the mobile ion concentration. Under SC conditions and low illumination, the LF semicircle is often not fully closed within the frequency range measured experimentally (until 100 mHz), which may introduce uncertainty in the extraction of the LF components ( $R_{LF}$  and  $C_{LF}$ ). Therefore, it is very important the experimental accuracy while analyzing extrapolated LF parameters. DD simulations were extended to lower frequencies (down to 0.1-1 mHz), enabling a more reliable estimation (see SI section S4, Fig. S4.16). However, when comparing simulations and experiments, uncertainties related to extrapolation and parameter correlation should be considered. Both experimental and simulated spectra were fitted using the same ECM, enabling a consistent extraction of circuitual elements, and a summary of the fitting parameters, including errors, is provided in the SI (Section S4, Tables S4.1–S4.4).



A shunt resistance  $R_{SH}$  was not explicitly included in the selected ECM, although it is included in the DD simulator. The contribution of  $R_{SH}$  to the resistive components ( $R_{HF}$  and  $R_{LF}$ ), which depends on bias and illumination conditions<sup>[25]</sup> is analyzed in the next sections. Further details on the measurement protocol, the impedance transfer function of the selected ECM (with and without  $R_{SH}$  element), and discussion of additional RC contributions reported for PSCs are provided in Section S2 of the SI.

### Analysis of $J$ - $V$ and SunsVoc characterization

Performance parameters extracted from  $J$ - $V$  measurements under 1 sun illumination are shown in **Fig. 3** and summarized in Table S3.1 of the SI. Experimental results (dots distributions) are compared with DD simulations (plots). Although  $V_{OC}$  values exceeding 1100 mV were achieved, reduced  $J_{SC}$  and FF limited the  $PCE$  compared with state-of-the-art inverted PSCs<sup>[39]</sup> (Table S3.2 of the SI). While FF losses are partly attributable to high series resistance ( $R_s$ ) and/or low shunt resistance ( $R_{SH}$ ), reduced  $J_{SC}$  may arise from optical or extraction losses<sup>[40]</sup>. DD simulations performed with fixed  $R_s$ ,  $R_{SH}$ , and photogeneration show that the performance limitations also originate from coupled effects of reduced carrier mobility and increased mobile  $N_{ion}$ , which seems governed by band offsets, captured via variations in  $V_{bi}$ .

Energy band offsets greater than 300 meV (low  $V_{bi}$ ) are detrimental for the  $PCE$ ,  $V_{OC}$  and FF in PSCs<sup>[13,14,40]</sup>. However, simulations (**Fig. 3 (a-c)**) reveal enhanced tolerance to such band offsets as  $N_{ion}$  increases from  $10^{15}$  to  $10^{19}$  cm<sup>-3</sup>, due to ionic screening that lowers interfacial barriers-even under forward bias (MPP and OC; SI section S4, Figs. S4.1 and S4.2), in line with other previous reports<sup>[19,20]</sup>. Yet, as shown in **Fig. 3 (d)**, at low  $\mu_{PK}$ , high  $N_{ion}$  hinders charge extraction and reduces the  $J_{sc}$ <sup>[40]</sup>, evidencing a trade-off between barrier screening and transport constraint. We note that for other device configurations with low doped CTLs and high interface recombination, an increase of the mobile ion concentration leads to a decrease of the  $PCE$ .



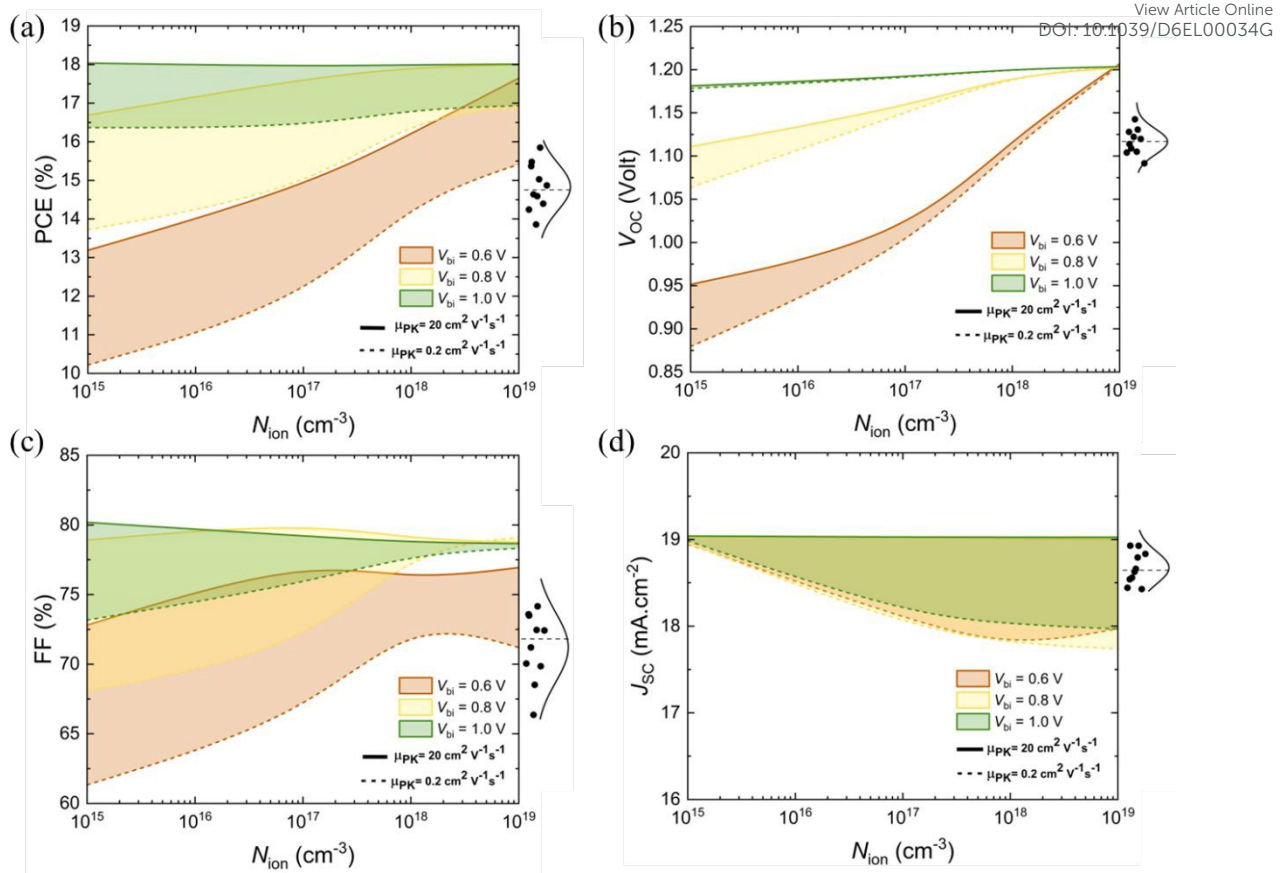


**Figure 3.** Simulated power conversion efficiency  $PCE$  (a), open-circuit voltage  $V_{OC}$  (b), fill factor  $FF$  (c) and short-circuit current  $J_{SC}$  (d), extracted from DD simulated  $J$ - $V$  curves assuming  $\tau_{PK}^{SRH}=1 \mu s$  and varying  $V_{bi}$  ( $V$ ) = {0.6, 0.8, 1}, within the ranges of high (solid lines) and low (dashed lines) electron-hole mobility  $\mu_{PK}$ . Side comparison with experimental results (black dots) with dashed horizontal lines indicating the median of the measured distributions.

Experimental dark  $J$ - $V$  curves and SunsVoc ( $J_{sc}$ - $V_{OC}$  points) measurements are presented in **Fig. 4 (a)**. Dark  $J$ - $V$  exhibit three regimes: shunt-dominated leakage at low bias ( $V < 0.6$  V), a recombination-controlled intermediate region, and  $R_S$ -limited saturation at high bias ( $V > 1.1$  V) when  $V_{bi}$  is surpassed and the injection of charge is significative. In the recombination regime, the current density ( $J_d$ ) follows the diode expression<sup>[41]</sup>:

$$J_d(V) = J_o \left( \exp \left[ \frac{qV_{int}}{n_{id}k_B T} \right] - 1 \right) \quad (1)$$

where  $k_B$  is the Boltzmann's constant,  $q$  the elementary charge,  $J_o$  the saturation current density pre-factor,  $n_{id}$  the ideality factor and  $T$  the temperature of the internal diode. The  $R_S$  induces  $V = V_{int} - J R_S$ , and the internal voltage,  $V_{int}$  approximates the quasi-Fermi level splitting ( $\Delta E_F/q$ )<sup>[11,42,43]</sup>. Therefore, Suns $V_{OC}$  measurements directly probe intrinsic recombination, as  $V_{OC} = V_{int}$  under OC conditions and a sufficiently large  $R_{SH}$ <sup>[8,9]</sup>. Experimental  $J_{sc}$ - $V_{OC}$  points



in **Fig. 4 (a)** closely reproduce the  $J_d$  profile without the  $R_s$  saturation effect towards high applied voltages.

An ideality factor  $n_{id}$  close to 2 (see SI, Tables S3.3 and S3.4) was obtained experimentally using **Eq. 1**, as shown in **Fig. 4 (a)** which suggests dominant SRH recombination<sup>[8,41,44]</sup>. In classic recombination theory for p-n junctions,  $n_{id} = 1$  indicates that the  $J$ - $V$  response is dominated by band-to-band recombination in the quasi-neutral regions, while  $n_{id} = 2$  correspond to dominant SRH recombination mediated by deep defects in the space charge region. In inverted PSCs, strong interfacial recombination may reduce the apparent  $n_{id}$  towards unity<sup>[7,17]</sup>. Within the DD framework, modifications of  $V_{bi}$ , via  $\Delta CB$  (PK/ETL),  $\Delta VB$  (PK/HTL), or interfacial  $N_{ion}$  accumulation, directly modulate carrier collection and modify the magnitudes of  $n_{id}$  and  $J_0$ <sup>[12]</sup>. As shown in **Fig. 4 (b)** the diode-regime recombination analysis is highly dependent on  $N_{ion}$ , complicating quantitative extraction of  $n_{id}$  in these devices.

Comparable  $n_{id}$  values were obtained from Suns $V_{OC}$  and dark  $J$ - $V$  curves (SI, Tables S3.3 and S3.4), whether extracted by linear regression or from the local derivative yielding the minimum  $n_{id}(V)$  as in **Fig. 4 (b)**, inset. As Suns $V_{OC}$  measurements largely eliminate  $R_s$  and  $R_{SH}$  contributions, recombination remains governed by minority carrier concentrations. Under illumination, high  $N_{ion}$  can therefore produce apparent  $n_{id}$  equal and above 2 (SI, Figure S4.3).

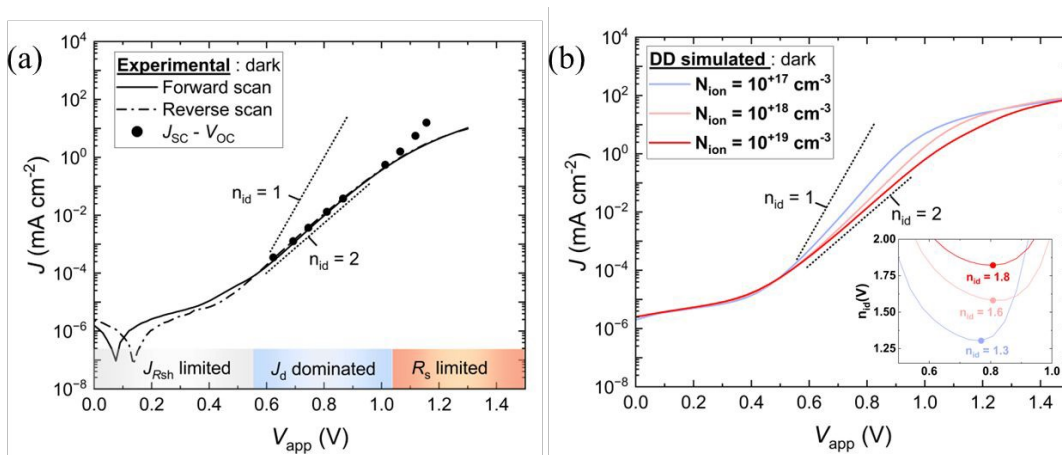


**Figure 4.** (a) Dark  $J$ - $V$ , in forward (solid) and reverse (dashed) sweep direction at  $30 \text{ mVs}^{-1}$ , directly compared with Suns $V_{OC}$  ( $J_{sc}$ - $V_{OC}$ ) points for recombination analysis at the diode-like current ( $J_d$ ) zone. (b) DD simulated dark  $J$ - $V$  curves (reverse scans), varying  $N_{ion}(\text{cm}^{-3}) = \{10^{17}, 10^{18}, 10^{19}\}$ , at  $\mu_{PK} = 0.2 \text{ cm}^2\text{V}^{-1}\text{s}^{-1}$ , low  $V_{bi}$  at  $0.6 \text{ V}$  ( $\Delta VB = 500 \text{ meV}$  and  $\Delta CB = 300 \text{ meV}$ ) and  $R_{SH} = 10^8 \Omega \text{ cm}^2$ . The  $n_{id}$  values of 1 and 2 were estimated using linear regression fits to Eq. 1 and from its local derivative minimum applied to the  $J$ - $V$  ( $n_{id}(V)$ ) inset in (b).



Consistent with the  $J$ - $V$  analysis, at a low  $\mu_{PK}$  and high band offsets, the tolerance effect at high  $N_{ion}$  cannot fully compensate recombination losses. Simulations show electron-hole concentration imbalances within the PK layer (see SI, Fig. S4.4) for large band offsets  $\Delta VB$  and  $\Delta CB$  at the at the PK/HTL and PK/ETL interface, respectively. These coupled interactions between band offsets and mobile ions, and their impact on recombination, are further examined through the comparison between experimental and simulated IS in the following sections.

### IS under Short-Circuit Conditions at Variable Illumination

To further interpret the device behavior,  $R_{HF}$  and  $R_{LF}$  are plotted as a function of  $J_{sc}$  in double-logarithmic representation, as is shown in **Fig. 5**, comparing experimental data with DD simulations varying  $\mu_{PK}$  and  $N_{ion}$ . Under SC conditions, the internal electric field, determined by  $V_{bi}$ , can be partially screened by mobile ion accumulation at the PK/CTL interfaces. However, varying  $V_{bi}$  from 0.6 to 1.0 V in the simulations does not produce significant changes in the resistive or capacitive response across the explored ranges of  $N_{ion}$  and  $\tau_{PK}^{SRH}$ . Noticeable deviations arise at low  $V_{bi}$  under transport-limited conditions (i.e. at lower  $\mu_{PK}$ ) in the PK as detailed in SI Fig S4.5.

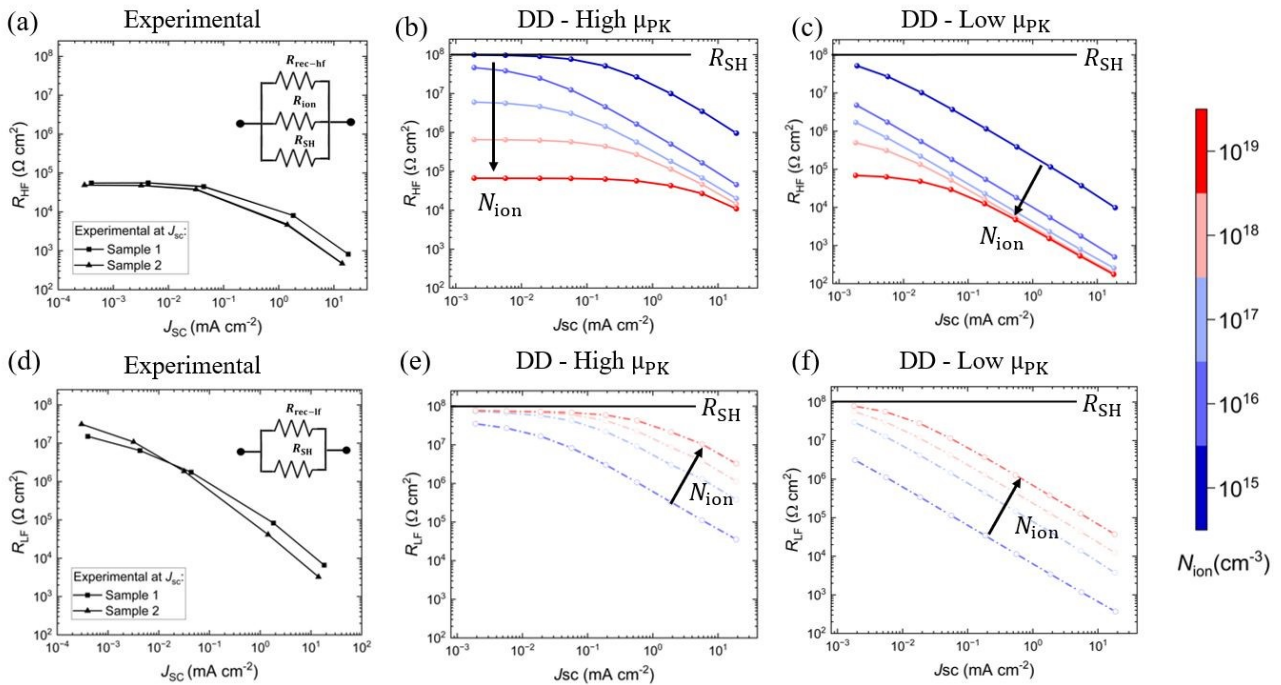


**Figure 5.**  $R_{HF}$  (a-c) and  $R_{LF}$  (d-f), as function of  $J_{sc}$  under increasing  $\Psi$  from  $1 \times 10^{-4}$  to 1 sun equivalent, extracted from IS fits to the selected ECM (as inset of Fig. 4 (d)). For DD simulations, the ion concentration varies in the range of  $N_{ion} = [10^{15} - 10^{19}] \text{ cm}^{-3}$ , with  $V_{bi} = 0.6 \text{ V}$ ,  $R_{SH} = 10^8 \text{ } \Omega \text{ cm}^2$  and  $\tau_{PK}^{SRH} = 1 \text{ } \mu\text{s}$ . Effect of increasing  $N_{ion}$  at high (b and e) vs low (c and f) electronic mobility,  $\mu_{PK} (\text{cm}^2 \text{V}^{-1} \text{s}^{-1}) = \{0.2, 20\}$ , respectively.



In general,  $R_{HF}$  and  $R_{LF}$  exhibit two distinct regimes as function of  $J_{sc}$ . At low  $\Psi$ , both resistances present an apparent plateau reaching a maximum value denoted here as  $R'_{SH}$ . At higher  $\Psi$ , they decrease linearly with increasing  $J_{sc}$ , consistent with a dominant recombination ( $R_{rec}$ ) associated with the enhanced photogenerated carrier density in the PK bulk. Accordingly, despite their different frequency origins (HF and LF), each resistance contribution can be independently described by a parallel combination of an effective  $R'_{SH}$  and an illumination intensity-dependent resistance  $R_{rec}(J_{sc})$ , expressed as follows:

$$R_{HF} = \frac{R'_{SH-HF} * R_{rec-HF}(J_{sc})}{R'_{SH-HF} + R_{rec-HF}(J_{sc})} \quad (2) \quad R_{LF} = \frac{R'_{SH-LF} * R_{rec-LF}(J_{sc})}{R'_{SH-LF} + R_{rec-LF}(J_{sc})} \quad (3)$$

Focusing on the  $R'_{SH-HF}$  plateaus in **Fig. 5 (a-c)**, we find that  $R_{HF}$  is affected by an additional resistive contribution ( $R_{ion}$ ) coming from the static  $N_{ion}$  distribution, which screens the internal electric field and remains effectively invariant within the HF perturbation range. The effect of mobile ions in the HF response has been often considered negligible in previous works [24–26,28]. For the PSC architecture investigated here, the combined IS and DD analysis suggests  $N_{ion}$  in the range of  $10^{18} - 10^{19} \text{ cm}^{-3}$ . In the case of low mobile ion concentration and ideally no shunt resistance, the plateau will come from a resistive dark recombination which will be in parallel to  $R_{ion}$ . This resistance  $R_{ion}$  is independent of illumination intensity and should be distinguished from the  $R_{rec-LF}$ , that is rather associated with additional modulation of recombination from slow ion motion in the LF range.

DD simulations also show that the slope of the linear  $R_{rec}$  decay, both at HF **Fig. 5 (b-c)** and LF in **Fig. 5 (e-f)**, is independent of the selected parameters. Additional simulated IS results (SI, Fig S4.6) explore  $\mu_{PK} = [0.2 - 20] \text{ cm}^2\text{V}^{-1}\text{s}^{-1}$  and  $\tau_{PK}^{SRH}$  from 10 ns to 1  $\mu\text{s}$ , spanning typical recombination rates reported for comparable PSC devices[20,30,45]. The illumination range in which  $R_{rec}$  predominates is strongly governed by  $\mu_{PK}$  and  $\tau_{PK}^{SRH}$  in the PK layer. Hence, we find that best agreement with experimental IS fits is obtained for medium-to-low mobilities of  $\mu_{PK} = [0.2-2] \text{ cm}^2\text{V}^{-1}\text{s}^{-1}$  and  $\tau_{PK}^{SRH} = 1 \mu\text{s}$ . A complementary analysis of IS fits, considering the impact of electron-hole mobility ( $\mu_e/\mu_h$ ) imbalances in the PK, can be found in SI section S4 (see **Fig S4.15**). Notably, the same  $R-J_{sc}$  profiles are obtained in DD simulations when varying  $\mu_{PK}$  and  $\tau_{PK}^{SRH}$  independently, as soon as their product  $\mu_{PK} \cdot \tau_{PK}^{SRH}$ , which determines a diffusion length  $L_D = \sqrt{D\tau}$ , remains constant for a given  $N_{ion}$ . This behavior arises from the implementation of the Einstein relation in the DD simulations, which couples mobility and diffusion coefficient. Towards dark conditions, where current is dominated by shunt-assisted leakage recombination, both  $R'_{SH-HF}$  and  $R'_{SH-LF}$  would be expected to converge toward  $R_{SH}$ ,



consistent with the  $J$ - $V$  analysis. Experimentally,  $R_{\text{HF}}$  and  $R_{\text{LF}}$  exhibit markedly different magnitudes at the lowest illumination ( $\Psi = 10^{-4}$  sun) as shown in **Fig. 5 (a) and (d)**. DD simulations at high  $\mu_{\text{PK}}$ , in **Fig. 5 (b) and (e)**, indicate that  $R_{\text{LF}}$  approaches the input  $R_{\text{SH}} = 10^8 \Omega \text{ cm}^2$  across all  $N_{\text{ion}}$ ; whereas  $R_{\text{HF}}$  progressively departs from  $R_{\text{SH}}$  with increasing  $N_{\text{ion}}$ . The pronounced divergence between  $R_{\text{HF}}$  and  $R_{\text{LF}}$  near dark conditions at 0 V bias suggests that the HF and LF responses are differently influenced by  $R_{\text{SH}}$ , mediated by ionic effects in the PK layer, ECMs in **Fig. 6 (a) and (b)**. From the maximum experimental  $R_{\text{LF}}$  values, the dark  $R_{\text{SH}}$  is estimated to be equal or higher than  $10 \text{ M}\Omega \text{ cm}^2$  (lower  $R_{\text{SH}}$  effects on simulated IS, shown in SI Fig. S4.7).

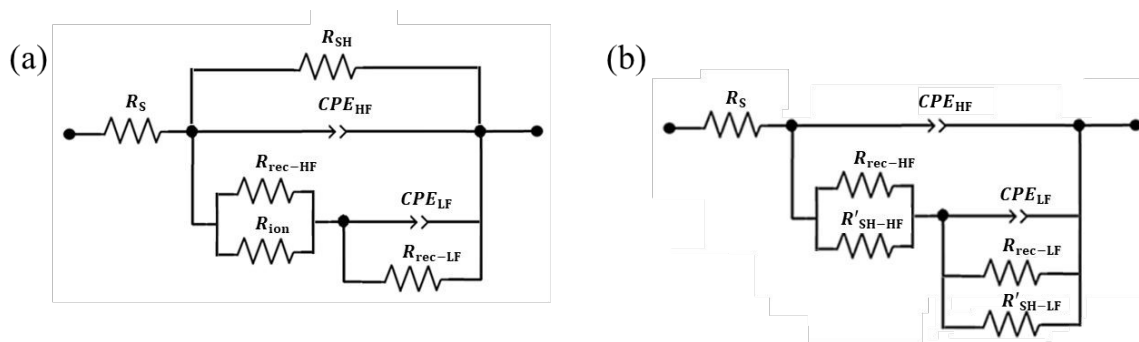
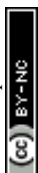


**Figure 6.** (a) Extended ECM proposed from the IS analysis of inverted PSCs in this study. It includes resistance dependence on the static  $N_{\text{ion}}$  distribution ( $R_{\text{ion}}$ ) at high frequencies, in parallel internal diode recombination ( $R_{\text{rec-HF}}$ ) and parasitic  $R_{\text{SH}}$ . At low frequencies, the diode recombination ( $R_{\text{rec-LF}}$ ) is modulated by mobile ions in the PK. (b) Equivalent structure, from the perspective of individual shunt effects, for high ( $R'_{\text{SH-HF}}$ ) and low ( $R'_{\text{SH-LF}}$ ) frequencies, resulting from a dynamic role of  $N_{\text{ion}}$  in the parasitic leakage currents, respectively.

It should be noted that the alternative ECMs proposed in **Fig. 6 (a-b)**, are not intended for a direct experimental implementation, as parallel resistive elements get reduced to a single equivalent resistance in the fitting process. Rather, they serve as a conceptual framework to illustrate the distinct physical contributions inherent to the  $R_{\text{HF}}$  and  $R_{\text{LF}}$  components, from the multiple “aggregated” ionic and electronic effects, as identified through DD simulations.

For  $R_{\text{LF}}$ , **Fig. 5 (d-f)**, increasing  $N_{\text{ion}}$  does not impact the  $R'_{\text{SH-LF}}$  plateau, but enhances  $R_{\text{rec-LF}}$  at high illumination. DD simulations indicate that internal bulk screening in the perovskite is reached for  $N_{\text{ion}} \sim 10^{17} \text{ cm}^{-3}$  (see SI, Fig S4.2) enabling ion redistribution under small LF perturbations. Consequently, the interfacial ion layer that contributes an additional  $R_{\text{ion}}$  at HF becomes less effective at LF due to ion migration. This is of particular importance because, for all the IS fits in this study, the magnitude of  $R_{\text{LF}}$  was always higher than that of  $R_{\text{HF}}$ , indicating that the LF contribution dominates the resistive component of the  $J$ - $V$  response

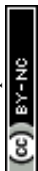


at  $J_{SC}$ . Similar trends have been reported in DD simulations of inverted PSCs, where  $N_{ion} > 10^{17} \text{ cm}^{-3}$  leads to an overall resistance increase (primarily dominated by  $R_{LF}$ ), and a concurrent reduction in the low frequency capacitance<sup>[30]</sup>. Importantly, as shown in Fig. 5,  $R_{LF}$  and  $R_{HF}$  exhibit opposite dependences on mobile ion concentration. An increase in  $N_{ion}$  reduces the HF resistance due to enhanced internal field screening, while it increases the LF resistance by modulating charge accumulation at the interfacial barriers. Complementary  $C$ - $J_{sc}$  profiles are included in the SI Fig S4.8.

Within the wide range of parameters explored in our simulations, the high frequency SC resistance in dark and under illumination shows a clear dependency with the recombination parameters and the mobile ion concentrations, given a sufficiently high shunt resistance. This suggests that, depending on the nature of the coupled capacitance, high frequency RC response times  $\tau_{HF}$  can be considered as a recombination lifetime. However, our analysis also indicates that the low frequency resistance in dark and low illumination SC conditions is governed by the shunt resistance and has no dependency on the concentration of mobile ions nor the recombination parameters (except high recombination rates). This implies that the RC response times  $\tau_{LF}$  associated with the corresponding dark low frequency process cannot be straightforwardly interpreted as a recombination lifetime. Furthermore, this also questions the nature of  $\tau_{LF}$  under illumination whose values typically are in the order of the dark  $\tau_{LF}$ . These findings are not only important for our general understanding of the recombination-related features of impedance spectra in PSCs, but they are particularly relevant for perovskite-based indoor photovoltaic and photodetector applications.

### IS under Open-Circuit Conditions at Variable Illumination

The combined protocol of IS measurements at OC, compared with DD-simulations, enables a refined recombination analysis by separating fast HF processes, where ionic profiles remain effectively frozen, from slower LF dynamics governed by ion redistribution. IS was measured at open-circuit conditions ( $V_{app} = V_{OC}$ ) increasing  $\Psi$  from  $10^{-4}$  up to 1 sun illumination, which corresponding to  $V_{OC} \approx 0.6 - 1.2 \text{ V}$  as presented in **Fig. 2 (b)** and **(d)**. Lower voltages ( $V_{OC} \leq 0.6 \text{ V}$ ) were not accessible due to instrumental limitations. At very low  $\Psi$ , the OC response is expected to give similar trends to the ones reported at SC, due to the reduction of electron and hole carrier concentrations in the PK bulk.



The resulting  $R$ - $V_{OC}$  plots present two regimes, analogously to the SC case and described using **Eq. 2** and **Eq. 3**.  $R_{HF}$ - $V_{OC}$  profiles are presented in **Fig. 7 (a-c)** ( $R_{LF}$ - $V_{OC}$  profiles are included in the SI section S4 Fig S4.12) for which the experimental IS data were fitted with DD simulations. We particularly highlight the impact of energy band offsets at the PK/HTL interface ( $\Delta VB$ , in **Fig. 1 (b)**), that modify  $V_{bi}$ , and mobile ion concentration, on the IS at OC. At low  $V_{OC} < 0.6$  V,  $R_{HF}$  displays a plateau  $R'_{SH-HF}$  consistent with a high  $R_{SH}$  ( $\sim 10^8 \Omega \text{ cm}^2$ ), with magnitude modulated by  $N_{ion}$  (see the effect of low  $R_{SH}$  under varying  $N_{ion}$ , in SI, Figure S4.13). At higher  $V_{OC}$ , once  $R_S$  and  $R_{SH}$  contributions are excluded and in the absence of strong injection/extraction barriers (resulting in a strong deviation of  $V_{int}$  from  $V_{app}$  [46]),  $R_{HF}$  is predominantly governed by diode recombination under flat-band conditions, following the characteristic exponential decay of  $R_{rec}$ [8]:

$$R_{rec} = \frac{n_{id} k_B T}{q J_o} \exp \left[ -\frac{q V_{OC}}{n_{id} k_B T} \right] \quad (4)$$

In line with the approach of Caprioglio, et al. [7,17], we evaluated the impact of  $\Delta VB$  on the recombination analysis by extracting  $n_{id}$ , from the  $R_{HF}$ - $V_{OC}$  slope (**Eq. 4**). Simulated IS fits were compared for moderate band offsets ( $\Delta VB = \Delta CB$  of 250 meV) and high band offsets ( $\Delta VB$  of 500 meV and  $\Delta CB$  of 300 meV) mainly at the PK/HTL interface. The corresponding cases, with  $V_{bi} = 0.9$  V and 0.6 V are shown in **Fig. 7 (b)** and **(c)**, respectively.

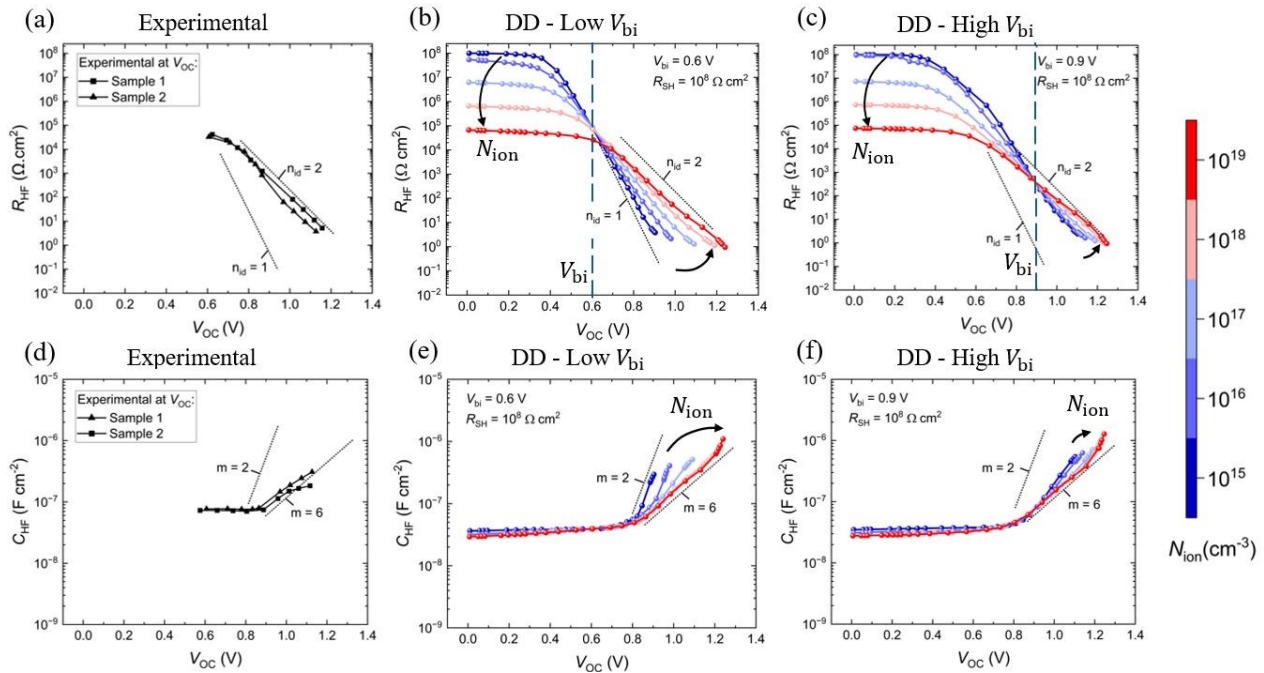


**Figure 7.**  $R_{HF}$  (a-c) and  $C_{HF}$  (d-f) in open-circuit conditions for different illumination intensities from  $10^{-4}$  up to 1 sun equivalent, obtained from IS fits to the selected ECM (inset in Fig. 2 (d)). Comparison of experimental IS



measurements in (a) and (d), versus DD simulations in (b-c) and (e-f) varying  $N_{\text{ion}}$  and  $V_{\text{bi}}$  at  $\tau_{\text{PK}}^{\text{SRH}} = 1 \mu\text{s}$ . The  $n_{\text{id}}$  and  $m$  reference values, indicated for the dashed lines, were determined using Eq. 4 and Eq. 5, respectively.

Comparing experimental data (**Fig. 7 (a)**) with DD simulations (**Fig. 7 (b-c)**) in the  $R_{\text{rec-HF}}$  decay regime at increasing  $V_{\text{oc}}$  reveals that higher  $N_{\text{ion}}$  leads to larger extracted  $n_{\text{id}}$  values, consistent with the dark  $J$ - $V$  analysis. Experimental  $n_{\text{id}}(\text{HF})$  values closer to 2 for representative devices confirm SRH-dominated recombination in the investigated PSCs. At the high  $N_{\text{ion}}$  range ( $10^{18}$ – $10^{19} \text{ cm}^{-3}$ ) identified under SC conditions, the electric field in the PK bulk becomes fully screened. Notably, at medium  $V_{\text{bi}}$  and high  $N_{\text{ion}}$ , the inflection point of  $R_{\text{HF}}-V_{\text{oc}}$  is at  $V_{\text{bi}}$ .

In PSCs, the resistance extracted from IS under OC conditions is commonly interpreted as electronic at HF, where ionic motion is effectively frozen, and as ion-modulated at LF due to ionic redistribution. The electronic resistance exclusively refers to the charge carriers (electrons and holes) that can follow the HF perturbation. In that sense, under OC conditions<sup>[31]</sup>, the HF response is governed by recombination consistent with diode behavior. However, even at HF, the resistance can be affected by the effect of mobile ions via field screening and modification of the charge density profile (as seen in Figure 7). Our results show that this “ionic-electronic contribution separation” is most valid at  $V_{\text{oc}}$  near flat-band conditions (Figure 7(b)-(c) dashed line), while deviations arise at lower illumination or away from  $V_{\text{bi}}$ . This approximation remains valid over a broader range of  $V_{\text{app}}$  approaching to  $V_{\text{bi}}$ , particularly in devices with higher  $V_{\text{bi}}$  (Figure 7(b-c)). Under OC, LF features arise from ion-induced modulation of the internal electric field (linked to  $V_{\text{bi}}$ , see Figure SI4.12) and interfacial charge accumulation. Notably, devices with larger  $V_{\text{bi}}$  exhibit a reduced dependence of  $R_{\text{LF}}$  on mobile ion concentration. In contrast, under SC conditions, both HF and LF resistive components are influenced by mobile ions through distinct mechanisms. At low illumination conditions the formation of a HF resistance plateau depends on the mobile ion concentration (if the electronic mobility is high enough), highlighting the impact of ionic screening on the nominally “electronic” response. At LF,  $R_{\text{LF}}$  is governed by interfacial charge accumulation and dependent of mobile ionic parameters. Therefore, the influence of mobile ions in both HF and LF resistances emphasizing the need for a unified ionic–electronic interpretation of IS spectra.

Experimental and simulated  $C_{\text{HF}}-V_{\text{OC}}$  are shown in **Fig. 7 (d-f)**. In all cases,  $C_{\text{HF}}$  exhibits a bias-independent contribution up to 0.9 V, corresponding to the total geometrical capacitance ( $C_{\text{geo}}^{\text{T}}$ ),



followed by a pronounced increase ( $\approx 2\text{--}5$  times within  $\sim 200$  mV), whose magnitude depends on  $V_{\text{bi}}$  and  $N_{\text{ion}}$ . Illustratively, a second sample also showed an apparent saturation towards a maximum at the same  $V_{\text{OC}} > 0.9$  V (**Fig. 7 (d)**). The monotonic increase is consistent with the onset of chemical-like electronic capacitance associated with carrier accumulation, whereas the saturation behavior may indicate additional parasitic contributions, such as contact depletion capacitance<sup>[36,37,47]</sup>. Although, additional effects from a temperature rise in the device during IS measurements at high  $\Psi$  cannot be fully excluded. As a first approximation,  $C_{\text{HF}}$  increases towards higher  $V_{\text{OC}}$  with an exponential function as follows:

$$C_{\text{HF}}(V) = C_0 \exp\left(\frac{qV}{m k_B T}\right) \quad (5)$$

where  $C_0$  corresponds to the chemical capacitance at dark equilibrium and  $m$  to the factor limiting the voltage-dependent activation related to electron and hole accumulation in the PK layer at a given forward bias condition<sup>[48]</sup>. The effective  $C_{\text{HF}}$  values presented in **Fig. 7 (d-f)**, were calculated following the fitting methodology presented in SI section S2 (equation S23). A summary of the IS fitting results is provided in Section S4 of the SI (Tables S4.1-S4.4). At HF, the  $CPE_{\text{HF}}$  fits generally present values of  $\alpha_{\text{HF}} > 0.91$ , indicating a response close to an ideal capacitance behavior, with a limited impact on the extracted  $C_{\text{HF}}$  and  $m_{\text{HF}}$  values.

From DD simulations in **Fig. 7 (e-f)**, we observe that the defined  $\Delta VB$  offset shifts the activation of  $C_{\text{HF}}(V)$  towards higher  $V_{\text{OC}}$ , likely by changing the activation factor  $m$  as in **Eq. 5**. For large  $\Delta VB$  (i.e., low  $V_{\text{bi}}$ ) at low  $N_{\text{ion}}$ , interfacial misalignment at the PK/HTL interfaces increases the hole injection barrier under high  $V_{\text{OC}}$ , leading to electron accumulation in the PK bulk (see SI, Fig. S4.4)<sup>[49]</sup>. Increasing  $N_{\text{ion}}$ , the injection barrier is effectively reduced due to ionic screening in the PK (see SI, Fig S4.12). The saturation of  $C_{\text{HF}}$  at high  $V_{\text{OC}}$  is also reproduced in DD simulations, particularly for the case of high energy band offsets (**Fig. 7 (e)**). Experimental extracted  $m$  values closer to 5 (**Fig. 7 (d)**) support the presence of high  $N_{\text{ion}}$  in the investigated PSCs. Although the parameter  $m$  can provide insight into the magnitude of  $N_{\text{ion}}$ , large extracted  $m$  values in an exponential fit may indicate that the capacitance-voltage dependence is not purely exponential, but instead associated with a transition between regimes and/or the overlap with polynomial or fractional space-charge capacitance contributions.

In this work, we do not include the analysis of additional inductive effects on performance loss, as reported in IS literature for some PSCs. For all the IS fits presented, as in **Fig. 2**,  $CPE$  values at HF and LF for the selected ECM displayed a dominant capacitive nature. However, we do



observe some incipient inductive signatures only towards limiting frequencies  $< 1$  Hz, for some experimental measurements under OC conditions at high illumination close to 1 sun. From DD simulations, we note that dominant inductive features, from mid to low frequencies (see SI section S4, Fig. S4.10), can emerge mainly under conditions where  $V_{OC} \approx V_{bi}$ , as reported in previous literature<sup>[32,50]</sup>. The inductive performance is associated with surface polarization and interfacial barriers that dynamically modulate charge injection and extraction under ion redistribution<sup>[51,52]</sup>, and that result in a phase delay between voltage and recombination currents<sup>[51,53,54]</sup>, consistent with an inductive response.

## Conclusion

By combining  $J$ - $V$ , SunsVoc, and multi-bias IS with drift-diffusion simulations, we conclude that the interplay between mobile ions and interfacial energy band offsets at perovskite/CTLs can limit the electronic transport and recombination in inverted (p-i-n) PSCs, ultimately impacting the device performance. Pronounced band offsets at the PK/CTL interfaces were identified as a key factor limiting FF and  $V_{OC}$ . Dark  $J$ - $V$  and SunsVoc analysis indicate high mobile ion concentrations ( $N_{ion} = 10^{18} - 10^{19} \text{ cm}^{-3}$ ) which enhance tolerance to interfacial band offsets and influence the extracted  $n_{id}$ . However, high  $N_{ion}$  values cannot fully compensate for reduced charge transport in the case of low carrier mobility in the perovskite ( $\mu_{PK} \sim 0.2 \text{ cm}^2 \text{ V}^{-1} \text{ s}^{-1}$ ).

IS measurements under both SC and OC conditions combined with DD simulations were performed under equivalent bias and illumination, enabled a consistent interpretation of the impedance response. Experimental and simulated IS spectra was fitted with a common ECM as function of  $J_{sc}$  and  $V_{oc}$ . IS under SC enabled an independent estimation of the electronic mobility ( $0.2 - 2 \text{ cm}^2 \text{ V}^{-1} \text{ s}^{-1}$ ), mobile ion concentration ( $10^{18} - 10^{19} \text{ cm}^{-3}$ ), and the dark shunt resistance ( $10^7 - 10^8 \Omega \text{ cm}^2$ ). Complementary OC at IS revealed distinct signatures of coupled ionic–electronic processes, linking resistive and capacitive responses to ion density and effective built-in voltage.

The role of mobile ion concentration was analyzed for both regimes, SC and OC. Under SC conditions, the high- and low-frequency resistances exhibit distinct dependencies on ion concentration, associated with ionic screening and interfacial charge accumulation, respectively, highlighting their different physical origins. At OC, the analysis reveals that the



high-frequency response approaches a purely electronic recombination regime near flat-band conditions influenced by the static ionic distribution, while low-frequency features reflect ion-modulated recombination. Simulations showed that the extracted ideality factor is also affected by the effective built-in voltage. Finally, we show that under dark conditions at 0V the  $R_{LF}$  resistance is dominated by the shunt resistance and is largely independent of recombination and ion density. Consequently, the associated  $RC$  time constant cannot be directly interpreted as a recombination lifetime.

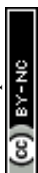
Overall, this integrated methodology provides a physically grounded framework to disentangle transport, recombination, and ionic effects in perovskite photovoltaics, offering guidance for interface optimization and device performance analysis.

## References

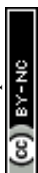
- <sup>1</sup> M.A. Green, E.D. Dunlop, M. Yoshita, N. Kopidakis, K. Bothe, G. Siefer, X. Hao, and J.Y. Jiang, “Solar Cell Efficiency Tables (Version 66),” *Prog. Photovolt. Res. Appl.* **33**(7), 795–810 (2025).
- <sup>2</sup> M.A. Green, A. Ho-Baillie, and H.J. Snaith, “The emergence of perovskite solar cells,” *Nat. Photonics* **8**(7), 506–514 (2014).
- <sup>3</sup> Y. Rakita, I. Lubomirsky, and D. Cahen, “When defects become ‘dynamic’: halide perovskites: a new window on materials?,” *Mater. Horiz.* **6**(7), 1297–1305 (2019).
- <sup>4</sup> S. Mazumdar, Y. Zhao, and X. Zhang, “Stability of Perovskite Solar Cells: Degradation Mechanisms and Remedies,” *Front. Electron.* **2**, 712785 (2021).
- <sup>5</sup> D.M. Atia, A.A. Hassan, H.T. El-Madany, A.Y. Eliwa, and M.B. Zahran, “Degradation and energy performance evaluation of mono-crystalline photovoltaic modules in Egypt,” *Sci. Rep.* **13**(1), 13066 (2023).
- <sup>6</sup> S.J. Robinson, A.G. Aberle, and M.A. Green, “Departures from the principle of superposition in silicon solar cells,” *J. Appl. Phys.* **76**(12), 7920–7930 (1994).
- <sup>7</sup> P. Caprioglio, C.M. Wolff, O.J. Sandberg, A. Armin, B. Rech, S. Albrecht, D. Neher, and M. Stollerfoht, “On the Origin of the Ideality Factor in Perovskite Solar Cells,” *Adv. Energy Mater.* **10**(27), 2000502 (2020).
- <sup>8</sup> O. Almora, K.T. Cho, S. Aghazada, I. Zimmermann, G.J. Matt, C.J. Brabec, M.K. Nazeeruddin, and G. Garcia-Belmonte, “Discerning recombination mechanisms and ideality factors through impedance analysis of high-efficiency perovskite solar cells,” *Nano Energy* **48**, 63–72 (2018).
- <sup>9</sup> P. Calado, D. Burkitt, J. Yao, J. Troughton, T.M. Watson, M.J. Carnie, A.M. Telford, B.C. O’Regan, J. Nelson, and P.R.F. Barnes, “Identifying Dominant Recombination Mechanisms in Perovskite Solar Cells by Measuring the Transient Ideality Factor,” *Phys. Rev. Appl.* **11**(4), 044005 (2019).
- <sup>10</sup> J.-F. Guillemoles, T. Kirchartz, D. Cahen, and U. Rau, “Guide for the perplexed to the Shockley–Queisser model for solar cells,” *Nat. Photonics* **13**(8), 501–505 (2019).
- <sup>11</sup> U. Würfel, D. Neher, A. Spies, and S. Albrecht, “Impact of charge transport on current–voltage characteristics and power-conversion efficiency of organic solar cells,” *Nat. Commun.* **6**(1), 6951 (2015).



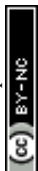
- <sup>12</sup> U. Rau, and T. Kirchartz, “Charge Carrier Collection and Contact Selectivity in Solar Cells,” *Adv. Mater. Interfaces* **6**(20), 1900252 (2019). Article Online  
DOI: 10.1039/D6EL00034G
- <sup>13</sup> C. Ding, Y. Zhang, F. Liu, Y. Kitabatake, S. Hayase, T. Toyoda, K. Yoshino, T. Minemoto, K. Katayama, and Q. Shen, “Effect of the conduction band offset on interfacial recombination behavior of the planar perovskite solar cells,” *Nano Energy* **53**, 17–26 (2018).
- <sup>14</sup> H.M. Pham, S.D.H. Naqvi, H. Tran, H.V. Tran, J. Delda, S. Hong, I. Jeong, J. Gwak, and S. Ahn, “Effects of the Electrical Properties of SnO<sub>2</sub> and C<sub>60</sub> on the Carrier Transport Characteristics of p-i-n-Structured Semitransparent Perovskite Solar Cells,” *Nanomaterials* **13**(24), 3091 (2023).
- <sup>15</sup> A. Bag, R. Pandey, S. Kashyap, J. Madan, and J. Ramanujam, “The influence of top electrode work function on the performance of methylammonium lead iodide based perovskite solar cells having various electron transport layers,” *Chem. Phys. Lett.* **806**, 140009 (2022).
- <sup>16</sup> T. Minemoto, and M. Murata, “Theoretical analysis on effect of band offsets in perovskite solar cells,” *Sol. Energy Mater. Sol. Cells* **133**, 8–14 (2015).
- <sup>17</sup> P. Caprioglio, M. Stollerfoht, C.M. Wolff, T. Unold, B. Rech, S. Albrecht, and D. Neher, “On the Relation between the Open-Circuit Voltage and Quasi-Fermi Level Splitting in Efficient Perovskite Solar Cells,” *Adv. Energy Mater.* **9**(33), 1901631 (2019).
- <sup>18</sup> J. Thiesbrummel, V.M. Le Corre, F. Peña-Camargo, L. Perdigón-Toro, F. Lang, F. Yang, M. Grischek, E. Gutierrez-Partida, J. Warby, M.D. Farrar, S. Mahesh, P. Caprioglio, S. Albrecht, D. Neher, H.J. Snaith, and M. Stollerfoht, “Universal Current Losses in Perovskite Solar Cells Due to Mobile Ions,” *Adv. Energy Mater.* **11**(34), 2101447 (2021).
- <sup>19</sup> W. Xu, L.J.F. Hart, B. Moss, P. Caprioglio, T.J. Macdonald, F. Furlan, J. Panidi, R.D.J. Oliver, R.A. Pacalaj, M. Heeney, N. Gasparini, H.J. Snaith, P.R.F. Barnes, and J.R. Durrant, “Impact of Interface Energetic Alignment and Mobile Ions on Charge Carrier Accumulation and Extraction in p-i-n Perovskite Solar Cells,” *Adv. Energy Mater.* **13**(36), 2301102 (2023).
- <sup>20</sup> L.J.F. Hart, F.J. Angus, Y. Li, A. Khaleed, P. Calado, J.R. Durrant, A.B. Djurišić, P. Docampo, and P.R.F. Barnes, “More is different: mobile ions improve the design tolerances of perovskite solar cells,” *Energy Environ. Sci.*, 10.1039.D4EE02669A (2024).
- <sup>21</sup> S. Baumann, “Stability and reliability of perovskite containing solar cells and modules: degradation mechanisms and mitigation strategies,” *Energy Env. Sci.*, (2024).
- <sup>22</sup> S.G. McCallum, O. Nicholls, K.O. Jensen, M.V. Cowley, J.E. Lerpinière, and A.B. Walker, “Bayesian parameter estimation for characterising mobile ion vacancies in perovskite solar cells,” *J. Phys. Energy* **6**(1), 015005 (2024).
- <sup>23</sup> T. Kirchartz, and B. Das, “Transforming characterization data into information in the case of perovskite solar cells,” *J. Phys. Energy* **5**(3), 031001 (2023).
- <sup>24</sup> E. Von Hauff, and D. Klotz, “Impedance spectroscopy for perovskite solar cells: characterisation, analysis, and diagnosis,” *J. Mater. Chem. C* **10**(2), 742–761 (2022).
- <sup>25</sup> A. Guerrero, J. Bisquert, and G. Garcia-Belmonte, “Impedance Spectroscopy of Metal Halide Perovskite Solar Cells from the Perspective of Equivalent Circuits,” *Chem. Rev.* **121**(23), 14430–14484 (2021).



- <sup>26</sup> C. Gonzales, A. Guerrero, and J. Bisquert, “Transition from Capacitive to Inductive Hysteresis: A Neuron-Style Model to Correlate  $I-V$  Curves to Impedances of Metal Halide Perovskites,” *J. Phys. Chem. C* **126**(32), 13560–13578 (2022). DOI: 10.1039/D6EL00034G
- <sup>27</sup> A.J. Riquelme, K. Valadez-Villalobos, P.P. Boix, G. Oskam, I. Mora-Seró, and J.A. Anta, “Understanding equivalent circuits in perovskite solar cells. Insights from drift-diffusion simulation,” *Phys. Chem. Chem. Phys.* **24**(26), 15657–15671 (2022).
- <sup>28</sup> E. Ghahremanirad, O. Almora, S. Suresh, A.A. Drew, T.H. Chowdhury, and A.R. Uhl, “Beyond Protocols: Understanding the Electrical Behavior of Perovskite Solar Cells by Impedance Spectroscopy,” *Adv. Energy Mater.* **13**(30), 2204370 (2023).
- <sup>29</sup> W. Clarke, G. Richardson, and P. Cameron, “Understanding the Full Zoo of Perovskite Solar Cell Impedance Spectra with the Standard Drift-Diffusion Model,” *Adv. Energy Mater.* **14**(32), 2400955 (2024).
- <sup>30</sup> O. Almora, P. López-Varo, R. Escalante, J. Mohanraj, L.F. Marsal, S. Olthof, and J.A. Anta, “Instability analysis of perovskite solar cells via short-circuit impedance spectroscopy: A case study on NiOx passivation,” *J. Appl. Phys.* **136**(9), 094502 (2024).
- <sup>31</sup> A. Riquelme, L.J. Bennett, N.E. Courtier, M.J. Wolf, L. Contreras-Bernal, A.B. Walker, G. Richardson, and J.A. Anta, “Identification of recombination losses and charge collection efficiency in a perovskite solar cell by comparing impedance response to a drift-diffusion model,” *Nanoscale* **12**(33), 17385–17398 (2020).
- <sup>32</sup> L.J. Bennett, A.J. Riquelme, and J.A. Anta, “Avoiding ionic interference in the computation of ideality factor for perovskite solar cells and an analytical theory for their impedance spectroscopy response,” (n.d.).
- <sup>33</sup> M. Nabil, I. Grau, R. Grau-Crespo, S. Hamad, and J.A. Anta, “Inversion of the Impedance Response Towards Physical Parameter Extraction Using Interpretable Machine Learning,” *Adv. Energy Mater.* **n/a**(n/a), e06352 (n.d.).
- <sup>34</sup> P. Calado, I. Gelmetti, B. Hilton, M. Azzouzi, J. Nelson, and P.R.F. Barnes, “Driftdiffusion: an open source code for simulating ordered semiconductor devices with mixed ionic-electronic conducting materials in one dimension,” *J. Comput. Electron.* **21**(4), 960–991 (2022).
- <sup>35</sup> J. Lim, M. Kober-Czerny, Y.-H. Lin, J.M. Ball, N. Sakai, E.A. Duijnste, M.J. Hong, J.G. Labram, B. Wenger, and H.J. Snaith, “Long-range charge carrier mobility in metal halide perovskite thin-films and single crystals via transient photo-conductivity,” *Nat. Commun.* **13**(1), 4201 (2022).
- <sup>36</sup> S. Ravishankar, Z. Liu, U. Rau, and T. Kirchartz, “Multilayer Capacitances: How Selective Contacts Affect Capacitance Measurements of Perovskite Solar Cells,” *PRX Energy* **1**(1), 013003 (2022).
- <sup>37</sup> S. Ravishankar, T. Unold, and T. Kirchartz, “Comment on ‘Resolving spatial and energetic distributions of trap states in metal halide perovskite solar cells,’” *Science* **371**(6532), eabd8014 (2021).
- <sup>38</sup> A. Lasia, “The Origin of the Constant Phase Element,” *J. Phys. Chem. Lett.* **13**(2), 580–589 (2022).
- <sup>39</sup> O. Almora, C.I. Cabrera, S. Erten-Ela, K. Forberich, K. Fukuda, F. Guo, J. Hauch, A.W.Y. Ho-Baillie, T.J. Jacobsson, R.A.J. Janssen, T. Kirchartz, M.A. Loi, X. Mathew, D.B. Mitzi, M.K. Nazeeruddin, U.W. Paetzold, B.P. Rand, U. Rau, T. Someya, E. Unger, L. Vaillant-Roca, and C.J. Brabec, “Device Performance of Emerging Photovoltaic Materials (Version 4),” *Adv. Energy Mater.* **14**(4), 2303173 (2024).



- <sup>40</sup> A. These, L.J.A. Koster, C.J. Brabec, and V.M. Le Corre, “Beginner’s Guide to Visual Analysis of Perovskite and Organic Solar Cell Current Density–Voltage Characteristics,” *Adv. Energy Mater.* **14**(21), 2400055 (2024). Article Online  
DOI: 10.1039/D6EL00034G
- <sup>41</sup> P. Würfel, and U. Würfel, “Chapter 6.4: The P-N Junction,” in *Phys. Sol. Cells Basic Princ. Adv. Concepts*, 3rd Edition, (Wiley-VCH Verlag GmbH & Co, 2016), pp. 132–145.
- <sup>42</sup> U. Rau, V. Huhn, and B.E. Pieters, “Luminescence Analysis of Charge-Carrier Separation and Internal Series-Resistance Losses in Cu ( In , Ga ) Se 2 Solar Cells,” *Phys. Rev. Appl.* **14**(1), 014046 (2020).
- <sup>43</sup> D. Grabowski, Z. Liu, G. Schöpe, U. Rau, and T. Kirchartz, “Fill Factor Losses and Deviations from the Superposition Principle in Lead Halide Perovskite Solar Cells,” *Sol. RRL* **6**(11), 2200507 (2022).
- <sup>44</sup> N.-P. Harder, “Chapter 3: Recombination processes in real materials,” in *Exp. Theor. Investig. Second Third Gener. Photovolt. Devices*, PhD Thesis, (Leipzig University, 2006), pp. 65–82.
- <sup>45</sup> M.A. Torre Cachafeiro, and W. Tress, “Ionic Losses and Gains in Perovskite Solar Cells: Impact on Efficiency and Stability,” *ACS Energy Lett.*, 4849–4855 (2025).
- <sup>46</sup> B. Tan, S.R. Raga, K.J. Rietwyk, J. Lu, S.O. Fürer, J.C. Griffith, Y.-B. Cheng, and U. Bach, “The impact of spiro-OMeTAD photodoping on the reversible light-induced transients of perovskite solar cells,” *Nano Energy* **82**, 105658 (2021).
- <sup>47</sup> A. Niemegeers, and M. Burgelman, “Effects of the Au/CdTe back contact on IV and CV characteristics of Au/CdTe/CdS/TCO solar cells,” *J. Appl. Phys.* **81**(6), 2881–2886 (1997).
- <sup>48</sup> J. Bisquert, “Chemical capacitance of nanostructured semiconductors: its origin and significance for nanocomposite solar cells,” *Phys. Chem. Chem. Phys.* **5**(24), 5360 (2003).
- <sup>49</sup> P. Lopez-Varo, J.A. Jiménez-Tejada, M. García-Rosell, J.A. Anta, S. Ravishankar, A. Bou, and J. Bisquert, “Effects of Ion Distributions on Charge Collection in Perovskite Solar Cells,” *ACS Energy Lett.* **2**(6), 1450–1453 (2017).
- <sup>50</sup> D. Zhang, A. Allagui, A.S. Elwakil, Z. Yan, and H. Lu, “Active circuit model of low-frequency behavior in perovskite solar cells,” *Org. Electron.* **85**, 105804 (2020).
- <sup>51</sup> E. Ghahremanirad, A. Bou, S. Olyae, and J. Bisquert, “Inductive Loop in the Impedance Response of Perovskite Solar Cells Explained by Surface Polarization Model,” *J. Phys. Chem. Lett.* **8**(7), 1402–1406 (2017).
- <sup>52</sup> D. Moia, I. Gelmetti, P. Calado, W. Fisher, M. Stringer, O. Game, Y. Hu, P. Docampo, D. Lidzey, E. Palomares, J. Nelson, and P.R.F. Barnes, “Ionic-to-electronic current amplification in hybrid perovskite solar cells: ionically gated transistor-interface circuit model explains hysteresis and impedance of mixed conducting devices,” *Energy Environ. Sci.* **12**(4), 1296–1308 (2019).
- <sup>53</sup> E. Ghahremani Rad, E.H. Balaguera, A.T. Gidey, K. Latosinsky, J. Bisquert, and A.R. Uhl, “Linking Double Inductance in Impedance Spectroscopy to Ionic Losses in Perovskite Photovoltaics,” *ACS Energy Lett.* **11**(4), 3211–3218 (2026).
- <sup>54</sup> E. H. Balaguera, and J. Bisquert, “Accelerating the Assessment of Hysteresis in Perovskite Solar Cells,” *ACS Energy Lett.* **9**(2), 478–486 (2024).



## Data availability

View Article Online  
DOI: 10.1039/D6EL00034G

The data supporting the findings of this study, including experimental measurements and device characterization data, are available within the article and its Supplementary Information. Additional raw data generated during the study are available from the corresponding authors upon reasonable request.

